

Effects of Energy Dissipation on Precursory Seismicity During Earthquake Preparation

Patrick Bianchi  *¹, Paul Antony Selvadurai  ¹, Luca Dal Zilio  ^{2,3}, Markus Rast  ⁴, Claudio Madonna  ⁴, Stefan Wiemer 

¹Swiss Seismological Service, ETH Zurich, Zurich, Switzerland, ²Earth Observatory of Singapore, Nanyang Technological University, Singapore, Singapore, ³Asian School of the Environment, Nanyang Technological University, Singapore, Singapore, ⁴Geological Institute, Department of Earth and Planetary Sciences, ETH Zurich, Zurich, Switzerland

Author contributions: *Formal Analysis:* Patrick Bianchi, Paul Antony Selvadurai, Luca Dal Zilio, Markus Rast, Stefan Wiemer. *Resources:* Claudio Madonna, Stefan Wiemer, Paul Antony Selvadurai. *Writing - Original draft:* Patrick Bianchi. *Writing - Review & Editing:* Patrick Bianchi, Paul Antony Selvadurai, Luca Dal Zilio, Markus Rast, Claudio Madonna, Stefan Wiemer. *Funding acquisition:* Stefan Wiemer, Claudio Madonna, Paul Antony Selvadurai.

Abstract The b -value of the magnitude distribution of natural earthquakes appears to be closely influenced by the faulting style (normal, thrust or strike-slip). We investigate this in the laboratory for the first time by analyzing the moment tensor solutions of acoustic emissions detected during a triaxial compression test on Berea sandstone. We observe systematic patterns showing that the faulting style influences the b -value and differential stress. Similar trends are observed in a complementary physics-based numerical model that captures mechanical energy dissipation. Both the differential stress and dissipation show to be inversely correlated to the b -value. The results indicate that, at late stages of the test, the dissipation increases and is linked to a change in acoustic emission (AE) faulting style and drop in b -value. The patterns observed in the laboratory Frohlich diagrams could be explained by the integrated earthquake model: damaged rock regions form as microcracks coalesce, leading to strain localization and runaway deformation. The modeling results also align with the micromechanics responsible for dissipation during the experiment and agrees with moment tensor solutions and petrographic investigations. The integration of physics-based models that can capture dissipative processes of the earthquake cycle could assist researchers in constraining seismic hazard in natural and anthropogenic settings.

Production Editor:

Yen Joe Tan

Handling Editor:

Matt Ikari

Copy & Layout Editor:

Tara Nye

Signed reviewer(s):

Georg Dresen

Received:

25 July 2024

Accepted:

11 November 2024

Published:

23 December 2024

1 Introduction

Researchers aim to predict the occurrence of earthquakes by identifying precursory signals linked to preparatory processes. In some cases these are observed as spatio-temporal variations of both seismic and aseismic parameters (e.g., Smalley et al., 1987; Turcotte, 1997; Brenguier et al., 2008; Gulia and Wiemer, 2019) and are associated with the localization of deformation (e.g., Bürgmann, 2014; Kato and Ben-Zion, 2020). Geodetic measurements have shown that aseismic deformation occurring near mainshock hypocenters correlated with increased seismic activity in several earthquake sequences (e.g., Kato et al., 2012; Obara and Kato, 2016). However, the interplay between large-scale processes and patterns in seismicity is still not well understood.

One of the ongoing debates in the seismological community is the use of spatio-temporal fluctuations of the b -value of the Gutenberg-Richter (GR) law (Gutenberg and Richter, 1944; Utsu, 1999)

$$\log_{10} N = a - bM \quad (1)$$

to individuate precursors to the next large earthquake (e.g., Gulia et al., 2016; Gulia and Wiemer, 2019). In

this equation, N represents the cumulative number of earthquakes with a moment magnitude equal to or greater than M , a is the frequency-magnitude intercept (or productivity term), and b is the slope, known as the b -value. A smaller b -value indicates a higher likelihood of larger earthquakes, while a larger b -value suggests a predominance of smaller earthquakes. Several studies have demonstrated an inverse proportionality between the b -value and the differential stress in laboratory experiments (Scholz, 1968; Amitrano, 2003; Goebel et al., 2013; Scholz, 2015; Meredith et al., 1990). This observation led to the inference that spatio-temporal fluctuations in b -values can be seen as “stress meters” within the subsurface (Schorlemmer et al., 2005). Further investigations demonstrated a dependence between the b -value and the stress regimes (i.e., extensional, compressional or strike-slip) experienced by faults in the field (Schorlemmer et al., 2005; Spada et al., 2013; Tormann et al., 2014; Petruccielli et al., 2019a,b). However, the debate about the use of b -value variations for earthquake forecasting remains, in a large part due to the statistical sensitivity and completeness of seismic catalogues. Developing a stronger connection between earthquake mechanics and statistical seismology will improve hazard assessment and operational earthquake forecasting.

*Corresponding author: patrick.bianchi@sed.ethz.ch

The b -value is determined by the maximum likelihood estimate of an exponential distribution as $b \times \ln 10 = (\bar{M} - M_c)^{-1}$ (Aki, 1965), where \bar{M} is the mean magnitude and M_c the magnitude of completeness of a given catalogue. M_c is a critical parameter because it increases during aftershock sequences due to close timing of subsequent events, which reduces the reliability of b -value at these moments (Knopoff et al., 1982; Kagan, 2004; Woessner and Wiemer, 2005; van der Elst, 2021). Recent work by van der Elst (2021) presented a method (b -positive) to determine the b -value based on magnitude differences that is less prone to completeness biases.

Another method that has been shown to provide valuable insights for investigating processes occurring before natural earthquakes and rock failure of laboratory samples is moment tensor analysis. Based on this approach, different studies have linked physical models to inelastic processes. Analytical investigations of the full moment-rate tensor have provided mathematical expressions to establish a connection between the observed seismic activity within a rock volume and the extent of damage (Ben-Zion and Ampuero, 2009; Ben-Zion and Lyakhovsky, 2019). Based on similar principles, Ben-Zion and Zaliapin (2020) suggested that main-shocks are caused by the coalescence of segmented damaged rock volumes separated by more competent material. During triaxial experiments conducted on different types of high-porosity sandstones (Kwiatek et al., 2014; Griffiths et al., 2019), moment tensor analysis was successfully employed to discern between acoustic emissions (AEs) produced by compaction bands (e.g., Menéndez et al., 1996; Fortin et al., 2005, 2006; Kwiatek et al., 2014; Heap et al., 2015; Brantut, 2018) from those involved in shear banding (Sondergeld and Estey, 1982; Nishizawa et al., 1984; Lockner, 1993; Kwiatek et al., 2014).

Anderson's faulting theory (Anderson, 1905) classifies faulting into three end-member styles (thrust/inverse, normal, and strike-slip faulting) based on the orientation of principal stress axes with respect to a reference direction (gravitational vector). The b -value and differential stress have shown distinct relationships with respect to the faulting style. Thrust faults exhibit low b -values and high differential stress, normal faults show high b -values and low differential stress, and strike-slip faults fall in between (Schorlemmer et al., 2005; Gulia and Wiemer, 2010; Petruccielli et al., 2018; Petruccielli, 2018; Petruccielli et al., 2019a,b). However, these studies have high uncertainties mainly due to the variability in the stress field that is notoriously difficult to constrain *in situ*. Performing similar investigations in laboratory settings, where the global stress can be directly measured and imposed, is crucial to improve our understanding of such relationships. Furthermore, developing and validating numerical models that can track a wide range of parameters, such as stress and both seismic and aseismic deformation, would complement the laboratory observations and may provide insights into the mechanisms governing earthquake preparatory processes.

The current paper results from a concerted experimental and modeling campaign to unravel a more prac-

tical link between the b -value and measurable field parameters. Bianchi et al. (2024) performed a failure test on a dry and intact sample of Berea sandstone in a triaxial setting by applying a confining pressure of 20 MPa and a constant piston displacement rate of 0.33 $\mu\text{m}/\text{s}$. Berea sandstone is a high porosity rock ($\phi = 19\%$) primarily composed of quartz (75%), feldspar (10%), phyllosilicates (10%) and carbonates (5%) (Zhang et al., 1990; Baud et al., 2004). The sample failed in a brittle manner producing a number of AEs recorded on an array of sixteen piezo-electric transducers (PZT). Brittle failure is modeled using the Hydro-Mechanical Earthquake Cycles code (H-MEC, Dal Zilio et al., 2022). H-MEC is a two-dimensions (x_1 - x_3 space, see Fig. 1a) fully coupled solid-fluid phase seismo-hydro-mechanical code governed by poro-elasto-viscoplastic rheology (Gerya, 2019; Yarushina and Podladchikov, 2015). During failure, accelerated deformation was observed as an increase in the bulk volumetric strain rate and the rate of AEs. A relationship between the average mechanical dissipation and these experimental metrics were clearly observed (Fig. 1c), lending credence to the model (Bianchi et al., 2024). Mechanical dissipation (equation 7 in Bianchi et al., 2024), a parameter directly linked to irreversible deformation, also showed a complex spatio-temporal distribution (see Fig. 1b) that explained the drop in seismic velocities and locations of AEs (Fig. 1d). This positive correlation between the numerical model and experimental results is further explored in this study. The reader is urged to consult Dal Zilio et al. (2022) for technical details regarding the numerical code and Bianchi et al. (2024) for the specifics of the numerical setup, boundary conditions and details on the experimental methodology.

Here, we augment the H-MEC framework by implementing the mobilized dilation angle model proposed by Zhao and Cai (2010). This improves the constitutive behavior as it incorporates a dilation response from initial stages to post-peak phases typically observed in triaxial failure tests. This addition is an important numerical development aimed at better describing bulk deformation and, potentially, the statistical seismic response.

This study aims at answering the following research questions: (1) Is the influence of the faulting style on the b -value also observable with AEs in the laboratory and under what assumptions? (2) Is it possible to relate fluctuations in b -values to a quantitative metrics of inelastic deformation (mechanical dissipation) determined from numerical models? (3) Can we gain insights into micromechanics in regions experiencing high-dissipation in the numerical modeling?

2 Methods

2.1 Calibration of the Piezo-Electric Transducers and Moment Tensor Solutions

To infer a physical understanding of AEs recorded by the PZTs, these sensors are absolutely calibrated (McLaskey and Glaser, 2012) and display a flat and broadband response between 100 kHz and 1.5 MHz

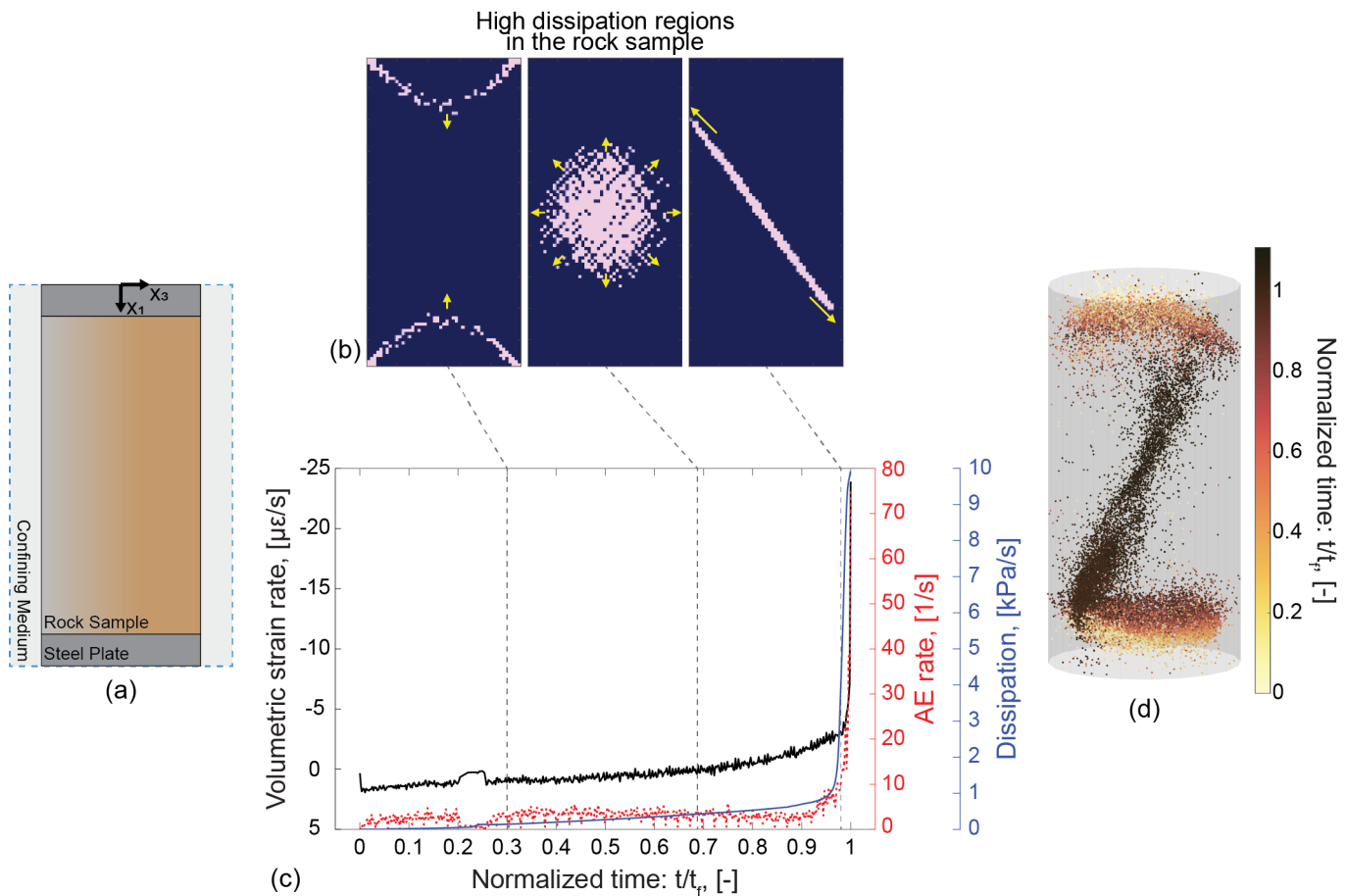


Figure 1 (a) Schematic of the numerical setup. (b) Regions of high dissipation (pink) at three snapshots in time of the simulations, where the yellow arrows indicate their spatio-temporal evolution. (c) Comparison of the volumetric strain rate, AE rate and simulated mean dissipation as a function of the normalized time to failure. (d) AE locations colored with respect to the normalized time to failure. (a), (b), (c) and (d) are adapted from [Bianchi et al. \(2024\)](#) (article licensed under CC BY 4.0).

(Proctor, 1982; Glaser et al., 1998; Selvadurai et al., 2022). Absolute calibration of the PZT sensors relies on using known sources applied to a transfer plate and spectral deconvolution of the theoretical displacement to infer the instrument response (Wu et al., 2021; Selvadurai et al., 2022). Instrument responses determined on the transfer plate are averaged in the frequency range 0.1–1 MHz, consecutively obtaining a single instrument response value for each PZT with units [V/m]. Coupling effects between the sensors and the specimen are neglected.

We use HybridMT (Kwiatek et al., 2016) to invert the catalogue of localized AEs (Bianchi et al., 2024) to obtain the moment tensor \mathbf{M} and moment magnitudes M_w (Vavryčuk, 2001, 2014). Following the methodology given by Kwiatek et al. (2016), we use the azimuth, take-off and incidence angles, the rock density, the distance between source and receivers, the P-wave velocity in the source region, the polarity of the first P-wave arrival and the low-frequency displacement plateau to construct the focal mechanism. The rock density and P-wave velocities are retrieved from Bianchi et al. (2024), whereas details concerning the azimuth, take-off and incidence angles are provided in the Supplementary Material 1. We note that in this study, we adopt the convention where compression is considered positive and extension is considered negative. We correct the ampli-

tude spectrum of the P-wave ground displacement with the averaged instrumental response of each sensor described above. This correction allows us to compute the low frequency displacement plateau Ω_0 (m/Hz) by averaging the corrected spectral amplitude values in the frequency range 100–500 kHz (McLaskey and Lockner, 2018).

The full seismic moment tensor \mathbf{M} is a 3×3 tensor that can be decomposed into its components given here as:

$$\mathbf{M} = \mathbf{M}_{ISO} + \mathbf{M}_{DC} + \mathbf{M}_{CLVD}, \quad (2)$$

where the \mathbf{M}_{ISO} is the isotropic component and the deviatoric component can be decomposed into a double-couple (\mathbf{M}_{DC}) and compensated linear vector dipole (\mathbf{M}_{CLVD}) (Vavryčuk, 2014). The ISO components denote the isotropic volumetric alteration from the seismic source. Negative values are interpreted to be crack closures (i.e., anticrack) or implosions, whereas positive values denote tensile crack opening or explosions. The CLVD components indicate motion towards or away from the earthquake source, without net volume change (Frohlich, 1994; Julian et al., 1996; Martínez-Garzón et al., 2017). The DC solutions are representative for pure shear motion obtained from two sliding blocks with opposite direction but of equal magnitude (e.g., Frohlich, 1994). \mathbf{M} can be decomposed using eigenval-

ues and an orthonormal basis eigenvector given as:

$$\mathbf{M} = M_1 \mathbf{e}_1 \mathbf{e}_1 + M_2 \mathbf{e}_2 \mathbf{e}_2 + M_3 \mathbf{e}_3 \mathbf{e}_3, \quad (3)$$

where $M_1 \geq M_2 \geq M_3$ and vectors \mathbf{e}_1 , \mathbf{e}_2 and \mathbf{e}_3 define P (pressure), B (intermediate or neutral) and the T (tension) axes, respectively. We choose to define the scalar seismic moment as the Frobenius norm (Silver and Jordan, 1982) in that

$$M_0 = \sqrt{\frac{1}{2} (M_1^2 + M_2^2 + M_3^2)}. \quad (4)$$

This follows the standard definition of scalar seismic moment given by Aki and Richards (2002) and can be expressed as the moment magnitude $M_w = (2/3)\log_{10}(M_0) - 6.02$ (Hanks and Kanamori, 1979), where M_0 has units [N·m].

To invert for the moment tensor solutions, we use the built-in function *focimt* (Kwiatek et al., 2016). For the moment tensor solutions, *focimt* provides their uncertainties, which are calculated as the normalized root-mean-square errors (RMS) between the observed and calculated P-wave amplitudes (Stierle et al., 2014b,a; Kwiatek et al., 2016):

$$\text{RMS} = \left(\frac{\sum_{i=1}^N (A_i^{\text{meas}} - A_i^{\text{exp}})^2}{\sum_{i=1}^N (A_i^{\text{meas}})^2} \right)^{1/2} \quad (5)$$

where i is one of N total sensors available for the inversion, A^{meas} is the P-wave amplitude measured and A^{exp} is the P-wave amplitude expected from the moment tensor inversion. Since not all sixteen PZTs simultaneously provided accurate wave arrival picks, events were located after discarding the waveforms associated with these inaccurate picks (Bianchi et al., 2024). For this reason, the number of available sensors for the inversion is variable and this affects the stability of the moment tensor solutions. We choose moment tensor results with $N \geq 12$ and $\text{RMS} \leq 0.40$ based on a robust analysis of the stability of the inversion solutions (McLaskey and Lockner, 2018).

2.2 Plunge-Based Ternary Diagrams in the Laboratory

We apply the same methodology presented in Petrucci et al. (2019b), where the relationship between the b -value and faulting style was compared using plunge-based ternary diagrams also referred to as a Frohlich diagram (Frohlich and Apperson, 1992; Frohlich, 2001). These diagrams communicate the faulting style associated with the double-couple (DC) component of the moment tensor and express the orientation of the principal stress axes P , B and T (Eqs. 2 and 3). P , B and T correspond to the eigenvectors of the moment tensors with associated eigenvalues in descending order of magnitude, respectively. The three axes of the Frohlich diagram describes the three plunge angles δ_P , δ_B and δ_T (0° – 90°), which defines the dip of the P , B and T axes.

The three plunge angles depend on the selected reference system, which for field studies is based on the widely employed North-East-Down (NED) coordinates.

In Supplementary Material 1 we provide the laboratory reference system used for our investigation. We define the North-East (Y-X) plane and the vertical (Z) axis to be perpendicular and parallel to the long axis of the sample, respectively. The origin of the laboratory reference system is located at the centre of the bottom end of the sample (see Supplementary Material 1). Each plunge angle is computed as the angles between the P , B and T axes and the X-Y plane. Later, we present comparisons of the laboratory results to the field observations of the Frohlich diagrams. We note that these should be treated with care due to the dependency of plunge angles on the reference system. However, the chosen laboratory reference system aligns with the stress axes imposed on the sample: the radial stress σ_r (or confining pressure, $P_c = \sigma_r = \sigma_2 = \sigma_3$) is aligned with the X-Y plane and the (principal) axial stress (σ_1) is aligned with the Z-axis. For this reason, even though a direct comparison between the faulting styles of laboratory and natural events is not fully consistent, our combined laboratory and modeling analysis can be complementary to the field observations as will be discussed.

To study the relationship between the mechanical dissipation and the faulting style, we carefully assign modeled dissipation values to the AEs (details are provided in Supplementary Material 2). We first collapse the experimental three-dimensional space with the locations of the AEs onto a two-dimensional plane to mimic the numerical domain (see Fig. 1a). To achieve similar time stamps, the experimental and numerical time vectors are normalized between the loading start and the sample failure t_f since the overall timing do not match perfectly (see section 2.5 in Bianchi et al., 2024). The AEs are then separated in time in groups centered around the numerical time steps t_{step} . For example, AEs detected in the time window 0.05 – 0.15 t/t_f are grouped within the time step $t_{\text{step}} = 0.10 t/t_f$, while those detected in the time window 0.15 – 0.25 t/t_f are grouped within $t_{\text{step}} = 0.20 t/t_f$ and so forth. The corresponding value of mechanical dissipation of a specific time step is then assigned from the closest numerical grid node to an individual AE. A differential stress value is also assigned to each event according to the macroscopic differential stress imposed at the associated time interval in which the event was detected.

We construct as many AE sub-catalogues as the number of DC sources displayed on the Frohlich diagram (12,105 moment tensor solutions). Each sub-catalogue is formed by a specific AE grouped together with its 500 closest events within the Frohlich's space (Petrucci et al., 2019b). For each sub-catalogue we determined the mean differential stress and mean dissipation by averaging the assigned values of the 501 events. Since the dissipation is a parameter that ranges over several orders of magnitude ($\sim 10^{-13}$ to 10^5 Pa·s $^{-1}$), we choose to average the logarithm of the assigned dissipation values instead of the absolute ones. A sensitivity analysis is performed to address the influence of the number of events per sub-catalogue on the influence of the faulting style and the results are provided in Supplementary Material 3. Three examples of sub-catalogues and their metrics (b -value, mean differential stress and mean dis-

sipation) are provided in the Supplementary Material 4.

2.3 Statistical Analysis of the Acoustic Emissions

For each sub-catalogue, the b -value is computed using the b -positive method (van der Elst, 2021), which relies on the distribution of positive magnitude differences. This method has been shown to be less prone to completeness biases than more conventional methods (e.g., Aki, 1965; Wiemer and Wyss, 2000). The b -value is determined by the maximum likelihood estimate for the Laplace distribution of positive magnitude differences as (van der Elst, 2021):

$$\begin{aligned} \beta &\cong \tilde{\beta} \\ &= \frac{1}{\Delta} \coth^{-1} \left[\frac{1}{\Delta} (\bar{M}' - M'_c + \Delta) \right] \end{aligned} \quad (6)$$

where $\beta = b \times \ln 10$, $\tilde{\beta}$ is the maximum likelihood estimate, Δ is the bin width used to discretize the positive magnitude differences, \bar{M}' is the mean of the positive magnitude differences and M'_c is the completeness value of positive magnitude differences. We assume $\Delta = 0.01$ corresponding to the level of accuracy we can achieve when estimating the absolute value of the moment magnitudes (e.g., Goebel et al., 2013). To determine M'_c we iteratively increase its value from 0.01 to 0.5 with steps of 0.01 and we evaluate the goodness of fit R (equation 2 in Wiemer and Wyss, 2000). This methodology estimates the absolute difference between the observed and predicted distributions of the number of magnitude differences in a specific bin and selects M'_c when $R > 90\%$ (Wiemer and Wyss, 2000). In this study M'_c equals 0.22 and is assumed to be constant for each sub-catalogue. The standard error δb of the b -value determined for each sub-catalogue is estimated following the formulation of Shi and Bolt (1982):

$$\delta b = \ln 10 \cdot b^2 \cdot \sqrt{\frac{\sum_i (M_i - \bar{M})^2}{N \cdot (N - 1)}}, \quad (7)$$

where N is the total number of events in each sub-catalogue and \bar{M} is the mean of the magnitudes M_i of each sub-catalogue.

2.4 Compaction and Dilation in H-MEC

H-MEC models the volumetric response of the porous rock matrix through the combination of three terms (Gerya, 2019; Dal Zilio et al., 2022): the reversible elastic (de)compaction $\zeta^{[el]}$, the irreversible visco-plastic compaction $\zeta^{[vp]}$ and the plastic dilation $\Gamma^{[pl]}$. We consider the strain rates of these components in the interest of this study. The three terms are mathematically defined as follows (Gerya, 2019; Petri et al., 2020; Dal Zilio et al., 2022):

$$\zeta^{[el]} = \frac{1}{K_d} \left(\frac{D^s p_t}{Dt} - \alpha \frac{D^f p_f}{Dt} \right) \quad (8)$$

$$\zeta^{[vp]} = \frac{p_t - p_f}{\eta_\phi (1 - \phi)} \quad (9)$$

$$\Gamma^{[pl]} = -2 \cdot \sin(\psi) \dot{\varepsilon}_{II}^{[pl]} \quad (10)$$

where p_t and p_f respectively are the total and fluid pressures, K_d is the drained bulk modulus, α is the Biot-Willis coefficient, $\frac{D^s(\cdot)}{Dt}$ and $\frac{D^f(\cdot)}{Dt}$ respectively are the Lagrangian time derivative in the solid and fluid reference frame, t is time, η_ϕ is the effective visco-plastic compaction viscosity, ϕ is the porosity, ψ is the dilation angle and $\dot{\varepsilon}_{II}^{[pl]}$ is the second invariant of the deviatoric plastic strain rate tensor. A positive compression and negative dilation convention is adopted here.

To more realistically capture the deformation in a triaxial setting, we implement the mobilized dilation angle model of Zhao and Cai (2010) within H-MEC. This model accounts for change in the dilation angle ψ with accumulated plastic shear strain. The relationship is phenomenological and has been obtained from several failure tests conducted at different confining pressures on seven lithologies (Zhao and Cai, 2010):

$$\psi = \frac{a \cdot b}{c - b} \cdot (\exp(-b \cdot \gamma^{[pl]}) - \exp(-c \cdot \gamma^{[pl]})) \quad (11)$$

where a , b and c are fitting coefficients dependent on the confining pressure P_c and on the rock lithology, and $\gamma^{[pl]}$ is the shear plastic strain (for more details see Supplementary Material 5). $\gamma^{[pl]}$ is defined as the difference between the axial and circumferential plastic strains, which are also the non-elastic components of the total strains (Zhao and Cai, 2010). H-MEC is constructed on an elasto-visco-plastic framework; therefore, we adjust the original formulated plastic shear strain $\gamma^{[pl]}$ to also include viscous terms in the new H-MEC definition:

$$\begin{aligned} \gamma^{[vp]} &= dt \cdot (\dot{\varepsilon}_{11}^{[vp]} - \dot{\varepsilon}_{33}^{[vp]}) \\ &= dt \cdot (\dot{\varepsilon}'_{11}^{[el]} - \dot{\varepsilon}'_{11}^{[el]} - \dot{\varepsilon}'_{33} + \dot{\varepsilon}'_{33}^{[el]}) \\ &= dt \cdot (\dot{\varepsilon}'_{11} - \dot{\varepsilon}'_{33}) - \frac{1}{2\mu} \cdot (\sigma'_{11} - \sigma'^0_{11} - \sigma'_{33} + \sigma'^0_{33}) \end{aligned} \quad (12)$$

where dt is the timestep, $\dot{\varepsilon}$ is the total strain rate, $\dot{\varepsilon}'$ is the deviatoric strain rate, μ is the shear modulus, σ' is the deviatoric stress and σ'^0 is the deviatoric stress of the previous timestep. The superscripts vp and el indicate the visco-plastic and elastic components of the strain rates, respectively, whereas the numbered subscripts 11 and 33 refer to the axial (x_1) and circumferential (x_3) directions, respectively. However, even though H-MEC includes a rheological model with viscosity-related terms, we assume these to be negligible in this study because of the brittle nature of laboratory tests at these environmental conditions (e.g., Menéndez et al., 1996). The simulations performed in this study, including the boundary conditions imposed, follow the same methodology presented in Bianchi et al. (2024). All parameters prescribed in the numerical model are provided in Supplementary Material 6.

3 Results

3.1 Temporal Evolution of Seismicity

Following the methodology in Section 2.1 and using the AE data from Bianchi et al. (2024), we obtain 12,105 mo-

ment tensor solutions that fit the criteria in Eq. 5. We then compute the moment magnitude M_w from Eq. 4 and in Fig. 2 we compare the events in time to the experimentally measured differential stress throughout the experiment. We show the normalized time to failure as in Fig. 1c. We see that seismicity is relatively constant, both in rate and maximum magnitude throughout the test. Only in the late stages ($t/t_f > 0.9$) the rate increases (see also Fig. 1c) but the maximum magnitude remains $M_w \leq -7$.

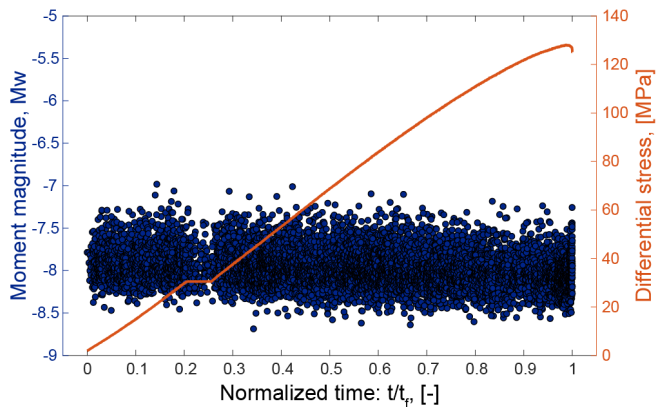


Figure 2 Temporal evolution of seismicity (blue markers) and differential stress (orange line) throughout the brittle failure test.

3.2 Double-Couple Moment Tensor Solutions

Figure 3 shows the DC component of the 12,105 moment tensor solutions displayed within three Frohlich diagrams (Figs. 3a, c and d) colored with respect to different parameters: the b -value (Fig. 3a), the mean differential stress (orange line in Fig. 2) measured from the triaxial apparatus (Fig. 3c) and the mean dissipation of mechanical energy retrieved from the numerical simulations (Fig. 3d). The b -value is calculated for each sub-catalogue as explained in Section 2.3, whereas we follow the methodology provided in Section 2.2 and Supplementary Material 2 to determine the mean mechanical dissipation and mean differential stress values. Figure 3b shows the DC moment tensor solutions of global earthquakes colored as a function of the b -value (retrieved from Petrucci et al., 2019b).

Systematic patterns are observed in each ternary diagram and show a significant degree of similarity among measurements retrieved in the laboratory (Figs. 3a and c), in the field (Fig. 3b), and numerically (Fig. 3d). In general, laboratory b -values are higher, which is common for AE studies (Lei et al., 1992; Lei and Ma, 2014). Higher laboratory b -values are also identified in the lower half of the ternary diagram, slightly shifted to the left towards the normal-faulting corner (see location (iii) on Fig. 3a). This trend is also observed in Fig. 3b, where the field b -values have a peak for similar sources according to the Frohlich diagrams. The minimum laboratory b -values are mainly observed at the top of the diagram corresponding to strike-slip sources. While this decrease in general trends are observed in field scale observations, the minimum field values (purple regions

where $b \sim 0.7$) is found towards the thrust faulting corner.

Overall the laboratory source coverage is lower in proximity of the two lower corners (normal and reverse faulting). The regions with higher b -values spatially correlate with regions showing lower differential stress. Similar trends are observed with the simulated mean dissipation (Fig. 3d), which also displays lower magnitudes in the same regions where higher b -values are found.

An important correlation becomes evident when comparing experimental differential stress to computational dissipation. Even though the mean dissipation is retrieved numerically, it still exhibits a similar pattern as observed experimentally. Here we find that thrust faulting is more often associated with high dissipation and occurs at higher differential stress, whereas the opposite is observed with normal-faulting. This trend is generally valid except for a region of the diagram located towards the normal faulting corner that exhibits high levels of both differential stress and dissipation (yellow regions on the left of the diagrams in Figs. 3c and d). Strike-slip events find themselves in between.

3.3 Full Moment Tensor Solutions

DC components of the moment tensor provide insights into the orientation and shear components of the rupture associated with an earthquake source but do not include any volumetric component of deformation. To complement our investigation we further provide the full moment tensor solutions of the same 12,105 AEs presented beforehand. Figure 4a shows the full moment tensor solutions of these events displayed on a Hudson net and colored by their probability density estimate (PDE). Figures 4b and c divide the AEs before and after the last ~ 6 minutes before the macrofracture nucleation ($t/t_f > 0.93$), respectively. Hudson nets are visual representations of the AE full moment tensor solutions and display the isotropic (ISO), compensated linear vector dipole (CLVD), and DC components in graphical form (Hudson et al., 1989; Knopoff and Randall, 1970). The probability density is determined by employing the kernel smoothing density function to compute the PDE over the full catalogue of AEs. This provides insight into the most common mechanisms within the full AE catalogue.

The majority of the AE source mechanisms (Fig. 4a) are found to be in the lower half of the Hudson net slightly towards the anticrack and negative linear vector dipole (LVD) regions, which are indicative of compressive source mechanisms. A fewer amount shows signs of LVD (+), CLVD (-), LVD(-) and CLVD (+) points, and also pure DC source types. Microseismicity (Tape and Tape, 2012b,a) and numerical models (van der Baan and Chorley, 2019) predict that, for materials with a Poisson's ratio below $\nu = 0.25$, the AE source mechanisms deviate from the diagonal line linking the LVD (+) and LVD (-) regions (Fig. 4c). Our sample exhibited a Poisson's ratio $\nu = 0.23$ (Bianchi et al., 2024), which explains these observations. The mechanisms associated with such events are partially indicative for shear motion but can also

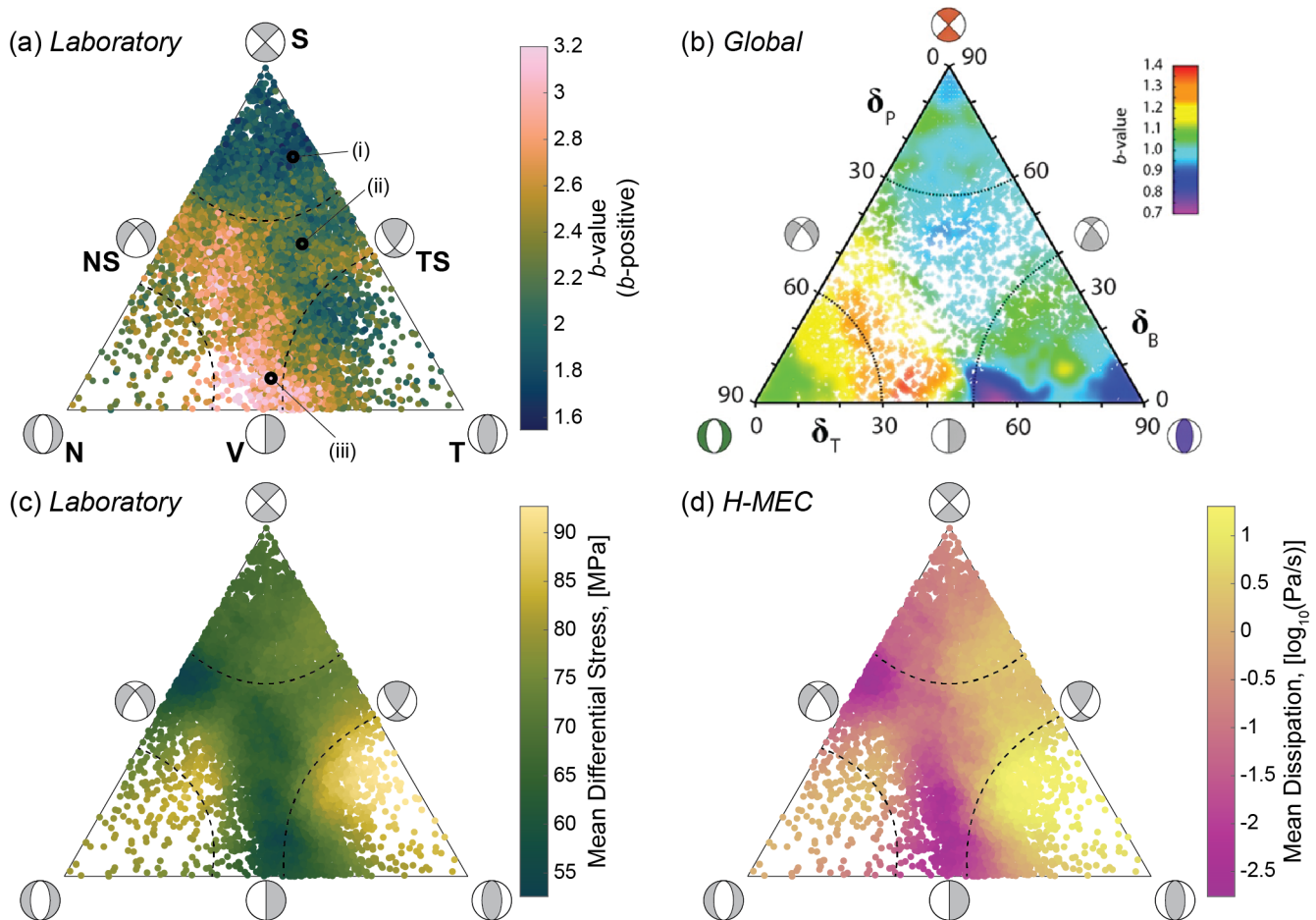


Figure 3 Plunge-based ternary diagrams showing the relationship between faulting style and (a) the b -value of the AE sub-catalogues (the limits of the colorbar are adjusted for visualization purposes), (b) the b -value of global earthquakes (retrieved from Petruccelli et al., 2019b); Typical faulting-style nomenclature is given: T – thrust; S – strike-slip; N – normal; V – vertical fault; TS – transpressional; NS – transtensional, (c) the mean differential stress measured during the laboratory test, and (d) the mean dissipation of mechanical energy simulated with H-MEC. More details of how the mean differential stress, mean dissipation and linking the experimentally observed AEs to H-MEC are provided in Supplemental Material 2. Three examples of frequency-magnitude distributions, differential stress and dissipation values for sub-catalogues exhibiting a (i) low, (ii) intermediate and (iii) high b -value are provided in Supplementary Material 4.

be representative for more complicated micromechanisms occurring at the grain scale.

4 Microstructural Observations

We perform a microscopical analysis of the post-mortem sample using a scanning electron microscope (SEM) with a back-scattered electron (BSE) detector to further investigate the AE source mechanisms (Fig. 4a). After dismantling of the test, we impregnated the sample with epoxy to maintain the microscopical structures. We prepared polished thin sections of $\sim 30 \mu\text{m}$ thickness by cutting rock sections of size $35 \times 20 \text{ mm}$ from the top and bottom ends of the sample. These sections were oriented along the central long axis of the sample and were extracted from the regions that observed AE clustering throughout the majority of the experiment (figure 5 in Bianchi et al., 2024) but away from the macrofracture.

Figure 4d shows three SEM-BSE micrographs with signatures of inelastic deformation. Studying micromechanical damage in this manner is a common tool to un-

derstand inelastic processes occurring at the grain scale in rock mechanics (Wong, 1982; Kranz, 1983). In Fig. 4d, we see strong evidence for grain crushing. Grain crushing and pore collapse are widespread throughout analyzed sections; however, the spatial distribution of damage is quite heterogeneous, where relatively intact regions mostly associated with grains cemented by carbonates exist next to highly damaged grains. Theory attributes grain crushing of this manner to the heterogeneity of contact forces in granular materials (Zhang et al., 1990) or shear induced pore collapse (Curran and Carroll, 1979). In Berea sandstone intragranular cracking, grain crushing, and pore collapse were intensely observed in uncemented grains (Menéndez et al., 1996). In the top, middle and bottom panels of Fig. 4d, we see evidence of crushing on a grain of quartz, feldspar and phyllosilicate, respectively.

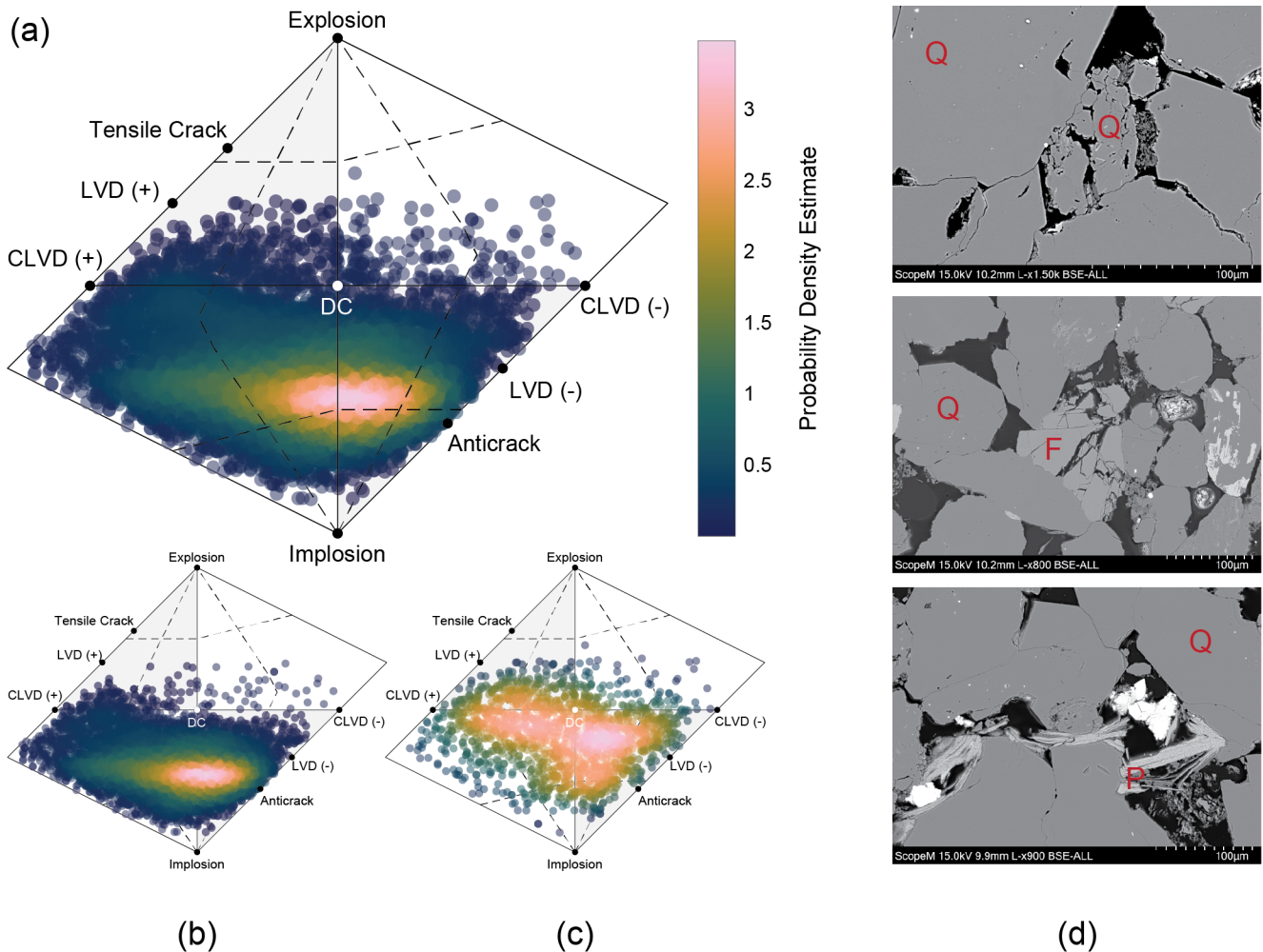


Figure 4 (a) Hudson net displaying the full moment tensor solutions of the AEs. Each point is colored by the spatial density of the nearby points. (b) Hudson net displaying the full moment tensor solutions of the events up to ~ 6 minutes before the macrofracture nucleation and (c) in the last ~ 6 minutes. (d) SEM-BSE micrographs. The top panel highlights crushing of a quartz grain, the middle panel highlights crushing of a feldspar grain and the bottom panel highlights crushing of a phyllosilicate grain. The main mineralogical components are indicated: quartz (Q), feldspar (F) and phyllosilicate (P).

5 Discussion

5.1 Fault Preparation, Accelerated Dissipation and Variations in b -value

The inverse proportionality of b -value with differential stress has been observed and studied in the laboratory (Scholz, 1968; Goebel et al., 2013, 2024). Goebel et al. (2013) discusses that at higher differential stress, seismic events have a higher probability of growing to larger sizes due to a general increase in stress level. Salazar Vásquez et al. (2024) observed a decrease in the b -value leading to brittle failure of an intact granite specimen that was also monitored using distributed strain sensing and AEs. This occurred at a slightly decreasing (albeit at a high) differential stress level. They found evidence of slow aseismic damage as the fault prepared to rupture. Salazar Vásquez et al. (2024) proposed that AEs occurring in these preparatory damaged regions have the potential to grow larger and have characteristic sizes that span the extent of the fragile damaged region (see also Dresen et al., 2020). This mechanism is also proposed to explain the drop in b -values with increasing strain rate in laboratory gouges (Bolton et al., 2021).

Considering that damage and inelastic deformation are synonymous, we further investigate the correlation between b -value, differential stress and mechanical dissipation.

We provide a quantitative comparison between the b -value and mean differential stress (Fig. 5a) and b -value and mean dissipation (Fig. 5b) of the sub-catalogues shown in Figs. 3a, c and d. To do so, we determine the Pearson correlation coefficients (Pearson, 1895) between the b -value and both the mean differential stress and mean dissipation, obtaining values equal to -0.42 and -0.51, respectively. These results are both indicative of a *moderate inverse correlation* (Schober et al., 2018). A best-fit linear regression is then applied to the b -values of each sub-catalogue (red lines, Figs. 5a and b) to quantitatively determine the relation between the two parameters. To integrate the uncertainty related to the b -value estimations (δb , Eq. 7) into the linear regression and provide a more robust statistical analysis, we weight each sub-catalogue by $1/\delta b^2$. Among all the sub-catalogues, δb is found within the range 0.097–0.412 with a mean of 0.191. Figure 5a shows the expected results, indicating that with increased differential stress

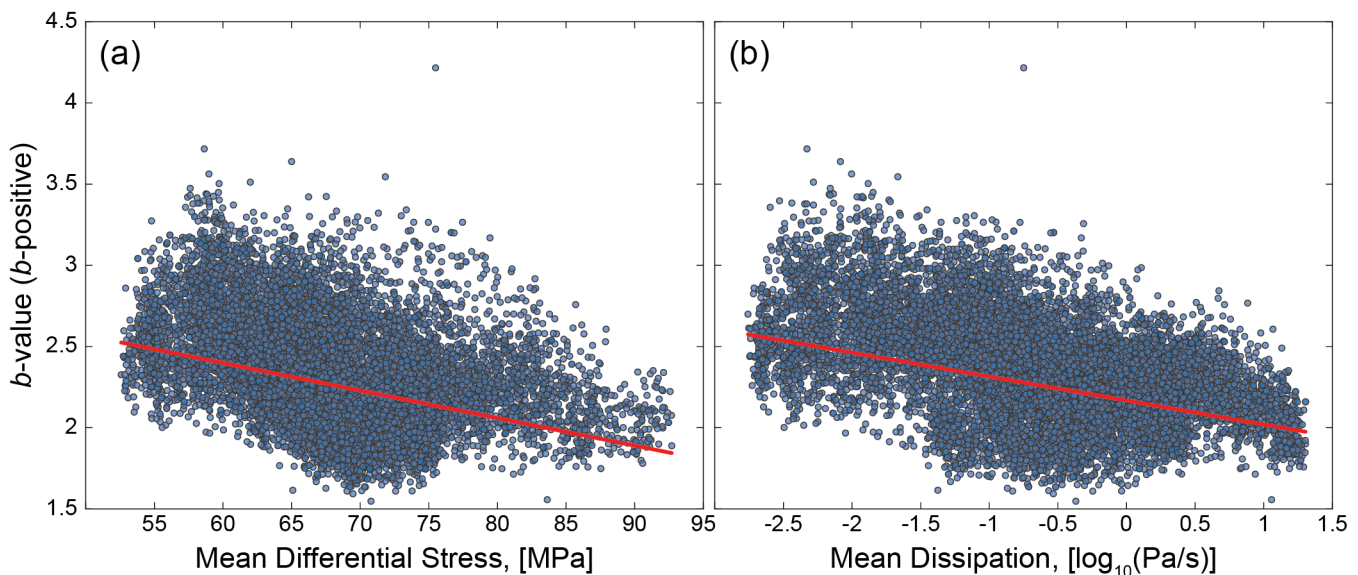


Figure 5 *b*-value (*b*-positive) as a function of the (a) mean differential stress and (b) mean dissipation of mechanical energy for each of the 12,105 AE sub-catalogues (blue dots). The red lines show the linear regressions weighted by $1/\delta b^2$ of each sub-catalogue.

there is a noted drop in the *b*-value. Comparing to the model, Fig. 5b also shows an inverse correlation between *b*-value and mechanical dissipation.

The mechanical dissipation is defined by the deviatoric strain rate times the deviatoric stress in the numerical framework (equation 7 in Bianchi et al., 2024). In the later stages of the numerical model ($t/t_f > 0.9$), the fault was observed to form, grow and accelerate, producing the marked increase in dissipation (Fig. 1c). We believe that this accelerated deformation is likely a feedback mechanism related to dissipation in the system: as a grouping of damaged material weakens during preparation, a small increase in differential stress will produce larger strain rates in this damaged volume and, by definition, dissipation will further weaken that volume. This results in more and faster weakening, which promotes the eventual localization of strain and formation of the main fault (Fig. 1b). The decrease in the *b*-value seems to be a marker for this damage feedback process that eventually leads to a runaway instability. This hypothesis is also consistent with other modelling efforts investigating *b*-value changes in the damage mechanics framework (Amitrano, 2003). These results suggest that while differential stress may show an inverse correlation with *b*-value, it may be a secondary effect and, decreases in *b*-value, may better explain the extent of damage (or localized damage) in a fault zone. Furthermore, previous laboratory investigations have already shown that the *b*-value may not be easily related to stress, as it was found to decrease even when the global stress remained constant or decreased slightly (Stanchits and Dresen, 2010).

Recent overviews on earthquake preparation have proposed it is hosted in a volumetric region where damage accumulates progressively, weakening the fault that hosts the mainshock (Kato and Ben-Zion, 2020; Martínez-Garzón and Poli, 2024). Integrated models that can account for bulk weakening and eventual ac-

celerated strain localization within the fault structure are considered important. In nature, *b*-value drops in regions of accelerated deformation have also been observed before Tohoku-Oki 2011 (Tormann et al., 2015; Nanjo et al., 2012) and also, to some significance level, before other seismic sequences (Gulia et al., 2016; Julia and Wiemer, 2019). Clustering of earthquakes have been proposed to explain broader weakening processes at tectonic scales (Ben-Zion and Zaliapin, 2020). There have been several geodetic observations in the field relating accelerated deformation to increased seismic activity (Kato and Nakagawa, 2014; Kato et al., 2012) and the eventual mainshock of a seismic series (e.g. Bürgmann, 2014). Similar geodetic techniques have also been used at the field (Sreejith et al., 2018) and reservoir scale (Julia, 2023) to investigate the correlation between deformation and the *b*-value; however, these observations are not universal (Stevens and Avouac, 2021). Other metrics to track the damaged clustering in a fault zone have been proposed, such as changes in radiated seismic energy (Ben-Zion and Ampuero, 2009) and decreases in seismic velocities (Ben-Zion and Lyakhovsky, 2019). Here we propose that fault preparation by dissipative (inelastic) processes may create conditions conducive to runaway rupture and a decrease in the *b*-value, controlled by these increasingly damaged and highly dissipative regions.

5.2 Micromechanics Associated with High-Dissipative Regions

To underpin the micromechanics responsible for damage and the numerically computed dissipation, we combine the numerical results with inferences from the full moment tensor solutions (Fig. 4a) and SEM-BSE micrographs (Fig. 4d). Figure 6 shows the numerical fields of the reversible elastic (de)compaction $\zeta^{[el]}$ (first column), irreversible compaction $\zeta^{[vp]}$ (second column),

dilation $\Gamma^{[pl]}$ (third column) and the overall volumetric response $\sum^{[vol]}$ (sum of the previous three terms, fourth column) within the sample. These terms represent strain rates and contribute to the overall dissipation within the sample. Sequential rows illustrate the progression of these fields across various phases of the simulated test: (Phase I) the post onset of yielding, (Phase II) during yielding, and (Phase III) at peak stress.

5.2.1 Phase I: Pore Compaction

Within the first phase, regions near the top and bottom of the sample display pronounced elastic compression rates. In this regime $\zeta^{[vp]}$ and $\Gamma^{[pl]}$ are also contributing to the overall volumetric response in similar regions. An overall compaction response emerges, particularly near the steel plates, aligning with high-dissipative regions identified in previous studies (Bianchi et al., 2024). Compressive AEs in these regions with shear compaction band formation have been observed in various experiments on high-porous sandstones (e.g., Menéndez et al., 1996; Fortin et al., 2005, 2006; Kwiatek et al., 2014; Heap et al., 2015; Brantut, 2018; Griffiths et al., 2019) and align with the AE mechanisms at this phase determined in this laboratory test (Fig. 4b).

Intragranular cracking, grain crushing and rearrangement are observed microscopically (Fig. 4d) and correspond to similar observations in studies on sandstone (Zhang et al., 1990; Menéndez et al., 1996; Shalev et al., 2014). Compressive AEs are physically interpreted as grain crushing and pore collapses that, as a consequence, result in the formation of compaction bands (e.g., Menéndez et al., 1996; Fortin et al., 2005, 2006; Kwiatek et al., 2014; Heap et al., 2015; Brantut, 2018). Grain rotation during this rearrangement can also induce dilation (Zhao et al., 2010), a feature also captured in our simulations (shown in $\Gamma^{[pl]}$ in column three of Fig. 6). As fragmented grains fill and settle in the pores, porosity decreases, leading to more compacted rock and enhanced intragranular grain cracking (Bernabe and Brace, 1990; Menéndez et al., 1996; Fortin et al., 2006; Shalev et al., 2014), further reducing porosity. Other numerical models corroborate this porosity reduction as a rock strengthening mechanism (Hamiel et al., 2005). This process leads to strain hardening, which subsequently inhibits strain localization (Menéndez et al., 1996).

5.2.2 Phases II-III: Shear Banding and Growth of a Fracture Plane

The yielding regime (second row in Fig. 6) reveals numerous sub-vertical structures that resemble shear bands (Menéndez et al., 1996; Fakhimi et al., 2006; Riedel and Labuz, 2006). Irreversible compaction and dilation manifest similar patterns and absolute values and mainly cluster in central region of the sample. At the peak stress (third row in Fig. 6), one dominant shear band localized into a macrofracture (Bianchi et al., 2024), with evident dilation along this interface juxtaposed to a balancing compacting region. The overall evolution of such shear mechanisms correlate with

the presence of shear-related AE source mechanisms (Fig. 4c).

Microstructural characterization performed by Menéndez et al. (1996) on several triaxial tests on Berea sandstone samples showed that shear-enhanced compaction lead to strain hardening in the samples and the development of shear localization. Comminution was also observed to occur within the shear bands and preceded cataclastic flow (Bernabe and Brace, 1990; Menéndez et al., 1996). During this process, grain boundaries are ruptured and, due to their rotation and settlement, this results in enhanced dilation (Menéndez et al., 1996; Riedel and Labuz, 2006). Our numerical results (third row of Fig. 6) also show a significant interplay between inelastic dilation and compaction that occurs about the dominant shear band, which supports the microstructures described by Menéndez et al. (1996) and the AE source mechanisms showed in Fig. 4c.

5.3 Transition of Faulting Style in Laboratory Failure Tests

The similarities at the laboratory and field scales (Figs. 3a and b) are interesting from a first-order comparison, but due to the dependence of these plots on the choice of reference system, it is not obvious how to simultaneously propose mechanisms that fit the observations at both scales. However, we can comment on the similarities between the numerical and experimental results and discuss possible mechanisms controlling the patterns of seismicity at different phases of the experiment.

We clearly see patterns and shifts in faulting style at lower and higher mean differential stress (green to yellow, in Fig. 3c). This implies that early in the experiment, AEs preferentially produce transtensional (TN) and vertical (V) style events. As the differential stress increases (closer to failure), there is a preference for thrust (T), transpressional (TS), and some normal (N) faulting. This transition is also associated with lower b -values as seen in Fig. 3a. This implies that larger events generally occur in the later stages, which can be explained by the overall increase in damage level (Katz and Reches, 2004; Salazar Vásquez et al., 2024) and the coalescence of microcracks forming interconnected and fragile networks as discussed in Section 5.1. The transition of the faulting style in these networks also tends to be more preferentially oriented toward the vertical component, i.e., the axis in which the principal stress (σ_1) is imposed.

The modeled dissipation (Fig. 3d) also shows that the earlier events (transtensional TN and vertical V) do not require high levels of dissipation to trigger them. However, once the damaged region grows and the strain rates therein increase (Bianchi et al., 2024), a changed preference for thrust (T), transpressional (TS) and some normal (N) faulting was observed in the later stages of the experiment and in the model. In this study, dissipation in the H-MEC model is only a proxy for where AEs may be generated. However, it appears to correlate well with a transition in source type with increased

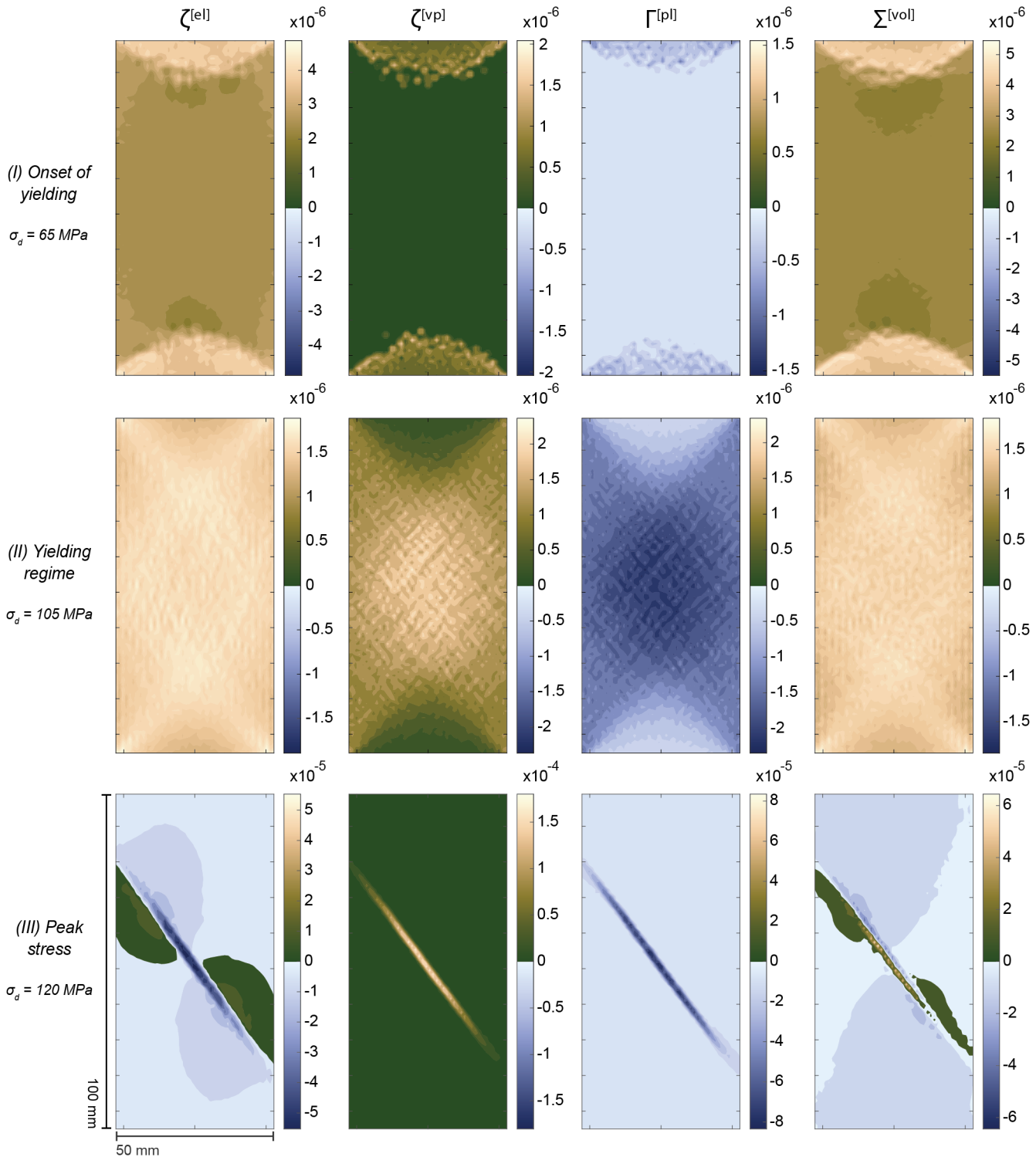


Figure 6 Numerical fields of the reversible elastic (de)compaction $\zeta^{[el]}$ (first column), irreversible compaction $\zeta^{[vp]}$ (second column), dilation $\Gamma^{[pl]}$ (third column) and the overall volumetric response $\sum^{[vol]}$ (fourth column) at three phases of the test within the sample: at the onset of yielding (first row), during the yielding regime (second row) and at the peak stress (third row). These three phases are displayed in a stress-strain representation in the Supplementary Material 7. All the plots share the same units [s^{-1}]. The positive colorbar indicates compression, whereas the negative one dilation.

localization. Similarities in source types in foreshock sequences (e.g. Diehl et al., 2017; Dodge et al., 1995; Bouchon et al., 2011; Brodsky and Lay, 2014) could potentially be an indicator of accelerated deformation in damaged zones of the fault, where fragile fault networks have become preferentially oriented with the stress field. This change in focal mechanism may in fact

be a precursory signal (Savage et al., 2017) but confirmation of these laboratory hypotheses at the field scale will require further investigations.

6 Conclusions

This study examined the influence of faulting style on the b -value of AEs detected during a triaxial failure test on Berea sandstone. We utilized numerical simulations with the H-MEC code to understand changes in the AE b -value associated with dissipation of mechanical energy. We also supported our hypotheses with evidence of the micromechanics and inelastic deformation responsible for this dissipation. We displayed the DC moment tensor solutions of the AEs in plunge-based ternary diagrams. Different parameters related to these AEs were investigated: *i*) the b -value, *ii*) the mean differential stress at which the AEs were detected and *iii*) the simulated mean mechanical dissipation. The results showed a systematic influence of the faulting style on these three parameters and shared similarities across different scales.

The correlation between the three different parameters controlling the formation of AEs and their faulting styles were investigated. Both mean differential stress and mean dissipation of mechanical energy were found to be inversely proportional to the b -value. We emphasize the potential of using the dissipation of mechanical energy to detect regions that may produce a main-shock. Dissipation produces irreversible deformation, which could be measured in the field using geodetic techniques. The numerical results indicate that, at late stages of the test (i.e., when differential stress is high), the mechanical dissipation increases in regions where strain is localizing onto a macro-fracture. This is linked to clear changes in faulting style and a drop in b -value. The patterns observed in the laboratory plunge-based ternary diagrams could be explained by the integrated earthquake model, which hypothesizes that damaged rock regions form as microcracks coalesce, leading to strain localization within a macro-fracture (or fault). The numerical model, in combination with microstructure analysis, helps to identify the micromechanisms responsible for the simulated dissipation. Pore compaction and shear banding emerged as the two dominant microscopic processes and these were consistent with both the full moment tensor solutions and the SEM analysis. H-MEC captured different physical processes that agree with previous observations at different scales and provided novel insights into the correlation between the AE b -value and the dissipation of mechanical energy. Whether these exact mechanisms play a significant role in natural fault zones settings remains to be confirmed but integrating such simulations in combination with seismic analysis may assist researchers in assessing hazard in both natural and anthropogenic scenarios.

Acknowledgements

The authors would like to acknowledge Dr. Antonio Pio Rinaldi and Dr. Danijel Schorlemmer for fruitful and insightful discussions on topics related to the presented investigation. We thank Antonio Salazar Vásquez, Sofia Michail and Hao Chen for the support provided during the implementation and dismantling

of the failure test and Thomas Mörgeli for his availability and technical support. Funding for P. Bianchi was provided from the Swiss National Science Foundation (SNSF) (No. 200021-192017). Partial funding for P. A. Selvadurai was provided from the European Research Council (ERC) project FEAR (grant 856559) under the European Community's Horizon 2020 Framework Programme Funds. L. Dal Zilio was supported by the European Research Council (ERC) Synergy Grant "Fault Activation and Earthquake Rupture" (FEAR) (No 856559), the Earth Observatory of Singapore (EOS), and the Singapore Ministry of Education Tier 3b project "Investigating Volcano and Earthquake Science and Technology (InVEST)" (Award No. MOE-MOET32021-0002). The authors would like to acknowledge the Swiss Seismological Service and the Swiss National Science Foundation with the project R'Equip206021-170766 - "Physical constraints on natural and induced earthquakes using innovative lab scale experiments: The LabQuake Machine".

Data and code availability

The laboratory and numerical data sets related to the investigations presented in this article are made open-source and can be retrieved from the following online repository: <https://doi.org/10.3929/ethz-b-000699560> (Bianchi, 2024).

Copyright Clearance

Figure 3b has been reprinted from "Earth and Planetary Science Letters, Vol. 527, Petruccielli A., Schorlemmer D., Tormann T., Rinaldi A.P., Wiemer S., Gasperini P., Vannucci G., *The influence of faulting style on the size-distribution of global earthquakes*, Page(s) 115791, Copyright (2019)" with permission from Elsevier.

Competing interests

The authors have no competing interests.

References

- Aki, K. Maximum likelihood estimate of b in the formula $\log N=a-bM$ and its confidence limits. *Bulletin of the Earthquake Research Institute, University of Tokyo*, 43:237–239, 1965. <https://cir.nii.ac.jp/crid/1573387450038851840>.
- Aki, K. and Richards, P. *Quantitative seismology*. University Science Books, 2 edition, 2002.
- Amitrano, D. Brittle-ductile transition and associated seismicity: Experimental and numerical studies and relationship with the b value. *Journal of Geophysical Research: Solid Earth*, 108(B1), Jan. 2003. doi: 10.1029/2001jb000680.
- Anderson, E. The dynamics of faulting. *Transactions of the Edinburgh Geological Society*, 8(3):387–402, Jan. 1905. doi: 10.1144/trans8.3.387.
- Baud, P., Klein, E., and Wong, T.-f. Compaction localization in porous sandstones: spatial evolution of damage and acoustic emission activity. *Journal of Structural Geology*, 26(4):603–624, Apr. 2004. doi: 10.1016/j.jsg.2003.09.002.

- Ben-Zion, Y. and Ampuero, J.-P. Seismic radiation from regions sustaining material damage. *Geophysical Journal International*, 178(3):1351–1356, Sept. 2009. doi: 10.1111/j.1365-246x.2009.04285.x.
- Ben-Zion, Y. and Lyakhovsky, V. Representation of seismic sources sustaining changes of elastic moduli. *Geophysical Journal International*, 217(1):135–139, Jan. 2019. doi: 10.1093/gji/ggz018.
- Ben-Zion, Y. and Zaliapin, I. Localization and coalescence of seismicity before large earthquakes. *Geophysical Journal International*, 223(1):561–583, June 2020. doi: 10.1093/gji/ggaa315.
- Bernabe, Y. and Brace, W. F. *Deformation and fracture of Berea sandstone*, page 91–101. American Geophysical Union, 1990. doi: 10.1029/gm056p0091.
- Bianchi, P. Dataset for the article "Effects of Energy Dissipation on Precursory Seismicity During Earthquake Preparation", 2024. doi: 10.3929/ETHZ-B-000699560.
- Bianchi, P., Selvadurai, P. A., Dal Zilio, L., Salazar Vásquez, A., Madonna, C., Gerya, T., and Wiemer, S. Pre-failure strain localization in siliciclastic rocks: A comparative study of laboratory and numerical approaches. *Rock Mechanics and Rock Engineering*, 57(8):5371–5395, June 2024. doi: 10.1007/s00603-024-04025-y.
- Bolton, D. C., Shreedharan, S., Rivière, J., and Marone, C. Frequency-magnitude statistics of laboratory foreshocks vary with shear Velocity, fault slip rate, and shear stress. *Journal of Geophysical Research: Solid Earth*, 126(11), Nov. 2021. doi: 10.1029/2021jb022175.
- Bouchon, M., Karabulut, H., Aktar, M., Özalaybey, S., Schmittbuhl, J., and Bouin, M.-P. Extended nucleation of the 1999 M_w 7.6 Izmit Earthquake. *Science*, 331(6019):877–880, Feb. 2011. doi: 10.1126/science.1197341.
- Brantut, N. Time-resolved tomography using acoustic emissions in the laboratory, and application to sandstone compaction. *Geophysical Journal International*, 213(3):2177–2192, Feb. 2018. doi: 10.1093/gji/ggy068.
- Brenguier, F., Campillo, M., Hadzioannou, C., Shapiro, N. M., Nadeau, R. M., and Larose, E. Postseismic relaxation along the San Andreas Fault at Parkfield from continuous seismological observations. *Science*, 321(5895):1478–1481, Sept. 2008. doi: 10.1126/science.1160943.
- Brodsky, E. E. and Lay, T. Recognizing foreshocks from the 1 April 2014 Chile earthquake. *Science*, 344(6185):700–702, May 2014. doi: 10.1126/science.1255202.
- Bürgmann, R. Warning signs of the Iquique earthquake. *Nature*, 512(7514):258–259, Aug. 2014. doi: 10.1038/nature13655.
- Curran, J. H. and Carroll, M. M. Shear stress enhancement of void compaction. *Journal of Geophysical Research: Solid Earth*, 84(B3):1105–1112, Mar. 1979. doi: 10.1029/jb084ib03p01105.
- Dal Zilio, L., Hegyi, B., Behr, W., and Gerya, T. Hydro-mechanical earthquake cycles in a poro-visco-elasto-plastic fluid-bearing fault structure. *Tectonophysics*, 838:229516, Sept. 2022. doi: 10.1016/j.tecto.2022.229516.
- Diehl, T., Kraft, T., Kissling, E., and Wiemer, S. The induced earthquake sequence related to the St. Gallen deep geothermal project (Switzerland): Fault reactivation and fluid interactions imaged by microseismicity. *Journal of Geophysical Research: Solid Earth*, 122(9):7272–7290, Sept. 2017. doi: 10.1002/2017jb014473.
- Dodge, D. A., Beroza, G. C., and Ellsworth, W. L. Foreshock sequence of the 1992 Landers, California, earthquake and its implications for earthquake nucleation. *Journal of Geophysical Research: Solid Earth*, 100(B6):9865–9880, June 1995. doi: 10.1029/95jb00871.
- Dresen, G., Kwiatek, G., Goebel, T., and Ben-Zion, Y. Seismic and Aseismic Preparatory Processes Before Large Stick-Slip Failure. *Pure and Applied Geophysics*, 177(12):5741–5760, Oct. 2020. doi: 10.1007/s00024-020-02605-x.
- Fakhimi, A., Riedel, J. J., and Labuz, J. F. Shear banding in sandstone: Physical and numerical studies. *International Journal of Geomechanics*, 6(3):185–194, May 2006. doi: 10.1061/(asce)1532-3641(2006)6:3(185).
- Fortin, J., Schubnel, A., and Guéguen, Y. Elastic wave velocities and permeability evolution during compaction of Bleurswiller sandstone. *International Journal of Rock Mechanics and Mining Sciences*, 42(7–8):873–889, Oct. 2005. doi: 10.1016/j.ijrmms.2005.05.002.
- Fortin, J., Stanchits, S., Dresen, G., and Guéguen, Y. Acoustic emission and velocities associated with the formation of compaction bands in sandstone. *Journal of Geophysical Research: Solid Earth*, 111(B10), Oct. 2006. doi: 10.1029/2005jb003854.
- Frohlich, C. Earthquakes with non—double-couple mechanisms. *Science*, 264(5160):804–809, May 1994. doi: 10.1126/science.264.5160.804.
- Frohlich, C. Display and quantitative assessment of distributions of earthquake focal mechanisms. *Geophysical Journal International*, 144(2):300–308, Feb. 2001. doi: 10.1046/j.1365-246x.2001.00341.x.
- Frohlich, C. and Apperson, K. D. Earthquake focal mechanisms, moment tensors, and the consistency of seismic activity near plate boundaries. *Tectonics*, 11(2):279–296, Apr. 1992. doi: 10.1029/91tc02888.
- Gerya, T. *Introduction to numerical geodynamic Modelling*. Cambridge University Press, May 2019. doi: 10.1017/9781316534243.
- Glaser, S. D., Weiss, G. G., and Johnson, L. R. Body waves recorded inside an elastic half-space by an embedded, wideband velocity sensor. *The Journal of the Acoustical Society of America*, 104(3): 1404–1412, Sept. 1998. doi: 10.1121/1.424350.
- Goebel, T. H. W., Schorlemmer, D., Becker, T. W., Dresen, G., and Sammis, C. G. Acoustic emissions document stress changes over many seismic cycles in stick-slip experiments. *Geophysical Research Letters*, 40(10):2049–2054, May 2013. doi: 10.1002/grl.50507.
- Goebel, T. H. W., Schuster, V., Kwiatek, G., Pandey, K., and Dresen, G. A laboratory perspective on accelerating preparatory processes before earthquakes and implications for foreshock detectability. *Nature Communications*, 15(1), July 2024. doi: 10.1038/s41467-024-49959-7.
- Griffiths, L., Dautriat, J., Vera Rodriguez, I., Iranpour, K., Sauvin, G., Park, J., Sarout, J., Soldal, M., Grande, L., Oye, V., Dewhurst, D. N., Haque Mondol, N., and Choi, J. C. Inferring microseismic source mechanisms and in situ stresses during triaxial deformation of a North-Sea-analogue sandstone. *Advances in Geosciences*, 49:85–93, Sept. 2019. doi: 10.5194/adgeo-49-85-2019.
- Julia, L. Time–space evolution of the Groningen Gas Field in terms of b-value: Insights and implications for seismic hazard. *Seismological Research Letters*, Apr. 2023. doi: 10.1785/0220220396.
- Julia, L. and Wiemer, S. The influence of tectonic regimes on the earthquake size distribution: A case study for Italy. *Geophysical Research Letters*, 37(10), May 2010. doi: 10.1029/2010gl043066.
- Julia, L. and Wiemer, S. Real-time discrimination of earthquake foreshocks and aftershocks. *Nature*, 574(7777):193–199, Oct. 2019. doi: 10.1038/s41586-019-1606-4.
- Julia, L., Tormann, T., Wiemer, S., Herrmann, M., and Seif, S. Short-term probabilistic earthquake risk assessment considering time-dependent b values. *Geophysical Research Letters*, 43

- (3):1100–1108, Feb. 2016. doi: 10.1002/2015gl066686.
- Gutenberg, B. and Richter, C. F. Frequency of earthquakes in California. *Bulletin of the Seismological Society of America*, 34(4): 185–188, 1944.
- Hamiel, Y., Lyakhovsky, V., and Agnon, A. Poroelastic damage rheology: Dilation, compaction, and failure of rocks. *Geochemistry, Geophysics, Geosystems*, 6(1), Jan. 2005. doi: 10.1029/2004gc000813.
- Hanks, T. C. and Kanamori, H. A moment magnitude scale. *Journal of Geophysical Research: Solid Earth*, 84(B5):2348–2350, May 1979. doi: 10.1029/jb084ib05p02348.
- Heap, M. J., Brantut, N., Baud, P., and Meredith, P. G. Time-dependent compaction band formation in sandstone. *Journal of Geophysical Research: Solid Earth*, 120(7):4808–4830, July 2015. doi: 10.1002/2015jb012022.
- Hudson, J. A., Pearce, R. G., and Rogers, R. M. Source type plot for inversion of the moment tensor. *Journal of Geophysical Research: Solid Earth*, 94(B1):765–774, Jan. 1989. doi: 10.1029/jb094ib01p00765.
- Julian, B. R., Ross, A., Foulger, G. R., and Evans, J. R. Three-dimensional seismic image of a geothermal reservoir: The Geysers, California. *Geophysical Research Letters*, 23(6):685–688, Mar. 1996. doi: 10.1029/95gl03321.
- Kagan, Y. Y. Short-term properties of earthquake catalogs and models of earthquake source. *Bulletin of the Seismological Society of America*, 94(4):1207–1228, Aug. 2004. doi: 10.1785/012003098.
- Kato, A. and Ben-Zion, Y. The generation of large earthquakes. *Nature Reviews Earth & Environment*, 2(1):26–39, Nov. 2020. doi: 10.1038/s43017-020-00108-w.
- Kato, A. and Nakagawa, S. Multiple slow-slip events during a foreshock sequence of the 2014 Iquique, Chile Mw 8.1 earthquake. *Geophysical Research Letters*, 41(15):5420–5427, Aug. 2014. doi: 10.1002/2014gl061138.
- Kato, A., Obara, K., Igashiki, T., Tsuruoka, H., Nakagawa, S., and Hirata, N. Propagation of slow slip leading up to the 2011 Mw 9.0 Tohoku-Oki Earthquake. *Science*, 335(6069):705–708, Feb. 2012. doi: 10.1126/science.1215141.
- Katz, O. and Reches, Z. Microfracturing, damage, and failure of brittle granites. *Journal of Geophysical Research: Solid Earth*, 109(B1), Jan. 2004. doi: 10.1029/2002jb001961.
- Knopoff, L. and Randall, M. J. The compensated linear-vector dipole: A possible mechanism for deep earthquakes. *Journal of Geophysical Research*, 75(26):4957–4963, Sept. 1970. doi: 10.1029/jb075i026p04957.
- Knopoff, L., Kagan, Y. Y., and Knopoff, R. *b* Values for foreshocks and aftershocks in real and simulated earthquake sequences. *Bulletin of the Seismological Society of America*, 72(5):1663–1676, Oct. 1982. doi: 10.1785/bssa0720051663.
- Kranz, R. L. Microcracks in rocks: A review. *Tectonophysics*, 100 (1–3):449–480, Dec. 1983. doi: 10.1016/0040-1951(83)90198-1.
- Kwiatek, G., Charalampidou, E.-M., Dresen, G., and Stanchits, S. An improved method for seismic moment tensor inversion of acoustic emissions through assessment of sensor coupling and sensitivity to incidence angle. *International Journal of Rock Mechanics and Mining Sciences*, 65:153–161, Jan. 2014. doi: 10.1016/j.ijrmms.2013.11.005.
- Kwiatek, G., Martínez-Garzón, P., and Bohnhoff, M. HybridMT: A MATLAB/Shell environment package for Seismic Moment Tensor Inversion and Refinement. *Seismological Research Letters*, 87(4):964–976, May 2016. doi: 10.1785/0220150251.
- Lei, X. and Ma, S. Laboratory acoustic emission study for earthquake generation process. *Earthquake Science*, 27(6):627–646, Dec. 2014. doi: 10.1007/s11589-014-0103-y.
- Lei, X., Nishizawa, O., Kusunose, K., and Satoh, T. Fractal structure of the hypocenter Distributions and Focal Mechanism Solutions of Acoustic Emission in Two Granites of Different Grain Sizes. *Journal of Physics of the Earth*, 40(6):617–634, 1992. doi: 10.4294/jpe1952.40.617.
- Lockner, D. The role of acoustic emission in the study of rock fracture. *International Journal of Rock Mechanics and Mining Sciences & Geomechanics Abstracts*, 30(7):883–899, Dec. 1993. doi: 10.1016/0148-9062(93)90041-b.
- Martínez-Garzón, P. and Poli, P. Cascade and pre-slip models oversimplify the complexity of earthquake preparation in nature. *Communications Earth & Environment*, 5(1), Mar. 2024. doi: 10.1038/s43247-024-01285-y.
- Martínez-Garzón, P., Kwiatek, G., Bohnhoff, M., and Dresen, G. Volumetric components in the earthquake source related to fluid injection and stress state. *Geophysical Research Letters*, 44(2): 800–809, Jan. 2017. doi: 10.1002/2016gl071963.
- McLaskey, G. C. and Glaser, S. D. Acoustic emission sensor calibration for absolute source measurements. *Journal of Nondestructive Evaluation*, 31(2):157–168, Jan. 2012. doi: 10.1007/s10921-012-0131-2.
- McLaskey, G. C. and Lockner, D. A. Shear failure of a granite pin traversing a sawcut fault. *International Journal of Rock Mechanics and Mining Sciences*, 110:97–110, Oct. 2018. doi: 10.1016/j.ijrmms.2018.07.001.
- Menéndez, B., Zhu, W., and Wong, T.-F. Micromechanics of brittle faulting and cataclastic flow in Berea sandstone. *Journal of Structural Geology*, 18(1):1–16, Jan. 1996. doi: 10.1016/0191-8141(95)00076-p.
- Meredith, P. G., Main, I. G., and Jones, C. Temporal variations in seismicity during quasi-static and dynamic rock failure. *Tectonophysics*, 175(1–3):249–268, Mar. 1990. doi: 10.1016/0040-1951(90)90141-t.
- Nanjo, K. Z., Hirata, N., Obara, K., and Kasahara, K. Decade-scale decrease in *b* value prior to the M9-class 2011 Tohoku and 2004 Sumatra quakes. *Geophysical Research Letters*, 39(20), Oct. 2012. doi: 10.1029/2012gl052997.
- Nishizawa, O., Onai, K., and Kusunose, K. Hypocenter distribution and focal mechanism of AE events during two stress stage creep in Yugawara andesite. *pure and applied geophysics*, 122 (1):36–52, Jan. 1984. doi: 10.1007/bf00879648.
- Obara, K. and Kato, A. Connecting slow earthquakes to huge earthquakes. *Science*, 353(6296):253–257, July 2016. doi: 10.1126/science.aaf1512.
- Pearson, K. Note on Regression and Inheritance in the Case of Two Parents. *Proceedings of the Royal Society of London Series I*, 58: 240–242, 1895.
- Petrini, C., Gerya, T., Yarushina, V., van Dinther, Y., Connolly, J., and Madonna, C. Seismo-hydro-mechanical modelling of the seismic cycle: Methodology and implications for subduction zone seismicity. *Tectonophysics*, 791:228504, Sept. 2020. doi: 10.1016/j.tecto.2020.228504.
- Petrucelli, A. *Universality of GR b-value gradients for different tectonic regimes and inferences on a differential stress dependence*. PhD thesis, alma, 2018. <http://amsdottorato.unibo.it/8466/>.
- Petrucelli, A., Vannucci, G., Lolli, B., and Gasperini, P. Harmonic fluctuation of the slope of the frequency-magnitude distribution (*b*-Value) as a function of the angle of rake. *Bulletin of the Seismological Society of America*, 108(4):1864–1876, June 2018. doi: 10.1785/0120170328.
- Petrucelli, A., Gasperini, P., Tormann, T., Schorlemmer, D., Rinaldi, A., Vannucci, G., and Wiemer, S. Simultaneous dependence

- of the earthquake-size distribution on faulting style and depth. *Geophysical Research Letters*, 46(20):11044–11053, Oct. 2019a. doi: 10.1029/2019gl083997.
- Petrucelli, A., Schorlemmer, D., Tormann, T., Rinaldi, A., Wiemer, S., Gasperini, P., and Vannucci, G. The influence of faulting style on the size-distribution of global earthquakes. *Earth and Planetary Science Letters*, 527:115791, Dec. 2019b. doi: 10.1016/j.epsl.2019.115791.
- Proctor, T. M. An improved piezoelectric acoustic emission transducer. *The Journal of the Acoustical Society of America*, 71(5): 1163–1168, May 1982. doi: 10.1121/1.387763.
- Riedel, J. J. and Labuz, J. F. Propagation of a shear band in sandstone. *International Journal for Numerical and Analytical Methods in Geomechanics*, 31(11):1281–1299, Dec. 2006. doi: 10.1002/nag.592.
- Salazar Vásquez, A., Selvadurai, P., Bianchi, P., Madonna, C., Germanovich, L. N., Puzrin, A. M., Wiemer, S., Giardini, D., and Rabaiotti, C. Aseismic strain localization prior to failure and associated seismicity in crystalline rock. *Scientific Reports*, 2024. doi: 10.1038/s41598-024-75942-9.
- Savage, H. M., Kieranen, K. M., P. Schaff, D., and Dieck, C. Possible precursory signals in damage zone foreshocks. *Geophysical Research Letters*, 44(11):5411–5417, June 2017. doi: 10.1002/2017gl073226.
- Schober, P., Boer, C., and Schwarte, L. A. Correlation coefficients: Appropriate use and interpretation. *Anesthesia & Analgesia*, 126 (5):1763–1768, May 2018. doi: 10.1213/ane.0000000000002864.
- Scholz, C. H. Microfracturing and the inelastic deformation of rock in compression. *Journal of Geophysical Research*, 73(4): 1417–1432, Feb. 1968. doi: 10.1029/jb073i004p01417.
- Scholz, C. H. On the stress dependence of the earthquake b value. *Geophysical Research Letters*, 42(5):1399–1402, Mar. 2015. doi: 10.1002/2014gl062863.
- Schorlemmer, D., Wiemer, S., and Wyss, M. Variations in earthquake-size distribution across different stress regimes. *Nature*, 437(7058):539–542, Sept. 2005. doi: 10.1038/nature04094.
- Selvadurai, P. A., Wu, R., Bianchi, P., Niu, Z., Michail, S., Madonna, C., and Wiemer, S. A methodology for reconstructing source properties of a conical piezoelectric actuator using array-based methods. *Journal of Nondestructive Evaluation*, 41(1), Feb. 2022. doi: 10.1007/s10921-022-00853-6.
- Shalev, E., Lyakhovsky, V., Ougier-Simonin, A., Hamiel, Y., and Zhu, W. Inelastic compaction, dilation and hysteresis of sandstones under hydrostatic conditions. *Geophysical Journal International*, 197(2):920–925, Mar. 2014. doi: 10.1093/gji/ggu052.
- Shi, Y. and Bolt, B. A. The standard error of the magnitude-frequency b value. *Bulletin of the Seismological Society of America*, 72(5):1677–1687, Oct. 1982. doi: 10.1785/bssa0720051677.
- Silver, P. G. and Jordan, T. H. Optimal estimation of scalar seismic moment. *Geophysical Journal of the Royal Astronomical Society*, 70(3):755–787, Sept. 1982. doi: 10.1111/j.1365-246x.1982.tb05982.x.
- Smalley, R. F., J., Chatelain, J.-L., Turcotte, D. L., and Prévot, R. A fractal approach to the clustering of earthquakes: Applications to the seismicity of the New Hebrides. *Bulletin of the Seismological Society of America*, 77(4):1368–1381, 1987. doi: 10.1785/BSSA0770041368.
- Sondergeld, C. H. and Estey, L. H. Source mechanisms and microfracturing during uniaxial cycling of rock. *pure and applied geophysics*, 120(1):151–166, Jan. 1982. doi: 10.1007/bf00879434.
- Spada, M., Tormann, T., Wiemer, S., and Enescu, B. Generic dependence of the frequency-size distribution of earthquakes on depth and its relation to the strength profile of the crust. *Geophysical Research Letters*, 40(4):709–714, Feb. 2013. doi: 10.1029/2012gl054198.
- Sreejith, K. M., Sunil, P. S., Agrawal, R., Saji, A. P., Rajawat, A. S., and Ramesh, D. S. Audit of stored strain energy and extent of future earthquake rupture in central Himalaya. *Scientific Reports*, 8(1), Nov. 2018. doi: 10.1038/s41598-018-35025-y.
- Stanchits, S. and Dresen, G. Advanced acoustic emission analysis of brittle and porous rock fracturing. *EPJ Web of Conferences*, 6: 22010, 2010. doi: 10.1051/epjconf/20100622010.
- Stevens, V. L. and Avouac, J.-P. On the relationship between strain rate and seismicity in the India–Asia collision zone: Implications for probabilistic seismic hazard. *Geophysical Journal International*, 226(1):220–245, Mar. 2021. doi: 10.1093/gji/ggab098.
- Stierle, E., Bohnhoff, M., and Vavryčuk, V. Resolution of non-double-couple components in the seismic moment tensor using regional networks—II: Application to aftershocks of the 1999 Mw 7.4 Izmit earthquake. *Geophysical Journal International*, 196(3): 1878–1888, Jan. 2014a. doi: 10.1093/gji/ggt503.
- Stierle, E., Vavryčuk, V., Šílený, J., and Bohnhoff, M. Resolution of non-double-couple components in the seismic moment tensor using regional networks—I: A synthetic case study. *Geophysical Journal International*, 196(3):1869–1877, Jan. 2014b. doi: 10.1093/gji/ggt502.
- Tape, W. and Tape, C. A geometric setting for moment tensors. *Geophysical Journal International*, 190(1):476–498, May 2012a. doi: 10.1111/j.1365-246x.2012.05491.x.
- Tape, W. and Tape, C. A geometric comparison of source-type plots for moment tensors: Plots of moment tensor source types. *Geophysical Journal International*, 190(1):499–510, May 2012b. doi: 10.1111/j.1365-246x.2012.05490.x.
- Tormann, T., Wiemer, S., and Mignan, A. Systematic survey of high-resolution b value imaging along Californian faults: Inference on asperities. *Journal of Geophysical Research: Solid Earth*, 119(3): 2029–2054, Mar. 2014. doi: 10.1002/2013jb010867.
- Tormann, T., Enescu, B., Woessner, J., and Wiemer, S. Randomness of megathrust earthquakes implied by rapid stress recovery after the Japan earthquake. *Nature Geoscience*, 8(2):152–158, Feb. 2015. doi: 10.1038/ngeo2343.
- Turcotte, D. L. *Fractals and chaos in geology and geophysics*. Cambridge University Press, July 1997. doi: 10.1017/cbo9781139174695.
- Utsu, T. Representation and analysis of the earthquake Size distribution: A historical review and some new approaches. *pure and applied geophysics*, 155(2–4):509–535, Aug. 1999. doi: 10.1007/s000240050276.
- van der Baan, M. and Chorney, D. Insights from micromechanical modeling of intact rock failure: Event characteristics, stress drops, and force networks. *Journal of Geophysical Research: Solid Earth*, 124(12):12955–12980, Dec. 2019. doi: 10.1029/2019jb018121.
- van der Elst, N. J. B -Positive: A robust estimator of aftershock magnitude distribution in transiently incomplete catalogs. *Journal of Geophysical Research: Solid Earth*, 126(2), Feb. 2021. doi: 10.1029/2020jb021027.
- Vavryčuk, V. Inversion for parameters of tensile earthquakes. *Journal of Geophysical Research: Solid Earth*, 106(B8):16339–16355, Aug. 2001. doi: 10.1029/2001jb000372.
- Vavryčuk, V. Moment tensor decompositions revisited. *Journal of Seismology*, 19(1):231–252, Oct. 2014. doi: 10.1007/s10950-014-9463-y.
- Wiemer, S. and Wyss, M. Minimum magnitude of completeness

- in earthquake catalogs: Examples from Alaska, the Western United States, and Japan. *Bulletin of the Seismological Society of America*, 90(4):859–869, Aug. 2000. doi: 10.1785/0119990114.
- Woessner, J. and Wiemer, S. Assessing the quality of earthquake catalogues: Estimating the magnitude of completeness and its uncertainty. *Bulletin of the Seismological Society of America*, 95(2):684–698, Apr. 2005. doi: 10.1785/0120040007.
- Wong, T.-F. Micromechanics of faulting in westerly granite. *International Journal of Rock Mechanics and Mining Sciences & Geomechanics Abstracts*, 19(2):49–64, Apr. 1982. doi: 10.1016/0148-9062(82)91631-x.
- Wu, R., Selvadurai, P. A., Chen, C., and Moradian, O. Revisiting piezoelectric sensor calibration methods using elastodynamic body waves. *Journal of Nondestructive Evaluation*, 40(3), Aug. 2021. doi: 10.1007/s10921-021-00799-1.
- Yarushina, V. M. and Podladchikov, Y. Y. (De)compaction of porous viscoelastoplastic media: Model formulation. *Journal of Geophysical Research: Solid Earth*, 120(6):4146–4170, June 2015. doi: 10.1002/2014jb011258.
- Zhang, J., Wong, T., and Davis, D. M. Micromechanics of pressure-induced grain crushing in porous rocks. *Journal of Geophysical Research: Solid Earth*, 95(B1):341–352, Jan. 1990. doi: 10.1029/jb095ib01p00341.
- Zhao, X. and Cai, M. A mobilized dilation angle model for rocks. *International Journal of Rock Mechanics and Mining Sciences*, 47(3):368–384, Apr. 2010. doi: 10.1016/j.ijrmms.2009.12.007.
- Zhao, X., Cai, M., and Cai, M. Considerations of rock dilation on modeling failure and deformation of hard rocks—a case study of the mine-by test tunnel in Canada. *Journal of Rock Mechanics and Geotechnical Engineering*, 2(4):338–349, 2010. doi: <https://doi.org/10.3724/SP.J.1235.2010.00338>.

The article *Effects of Energy Dissipation on Precursory Seismicity During Earthquake Preparation* © 2024 by Patrick Bianchi is licensed under CC BY 4.0.